

# Comparative Colorimetric Simulation and Evaluation of Digital Cameras Using Spectroscopy Data

Cong Phuoc Huynh<sup>1</sup> and Antonio Robles-Kelly<sup>1,2</sup>

<sup>1</sup>RSISE, Bldg. 115, Australian National University, Canberra ACT 0200, Australia

<sup>2</sup>National ICT Australia (NICTA)\*, Locked Bag 8001, Canberra ACT 2601, Australia

## Abstract

*In this paper, we present a comparative simulation and evaluation of digital cameras using spectroscopy, colorimetry and photogrammetry. Here, we compare the output of commercially available cameras to that yielded using the CIE-1931 colour standard and the colour matching functions proposed by Stiles and Burch [14]. We present a method to estimate the colour yielded by trichromatic cameras based upon their spectral response. We then present the results on three experimental vehicles and three commercially available cameras. We perform simulation using the spectrum of light emitted by black body radiators, the spectra of sample colours widely used for colour correction and present renderings using the spectra of known materials under controlled illumination conditions.*

## 1 Introduction

In computer vision, video and graphics, we rely upon cameras and rendering contexts to capture and reproduce colour information. The simulation and evaluation of this information is of capital importance to understand and predict the relation between the scene and the camera image. Moreover, the accurate capture and reproduction of colours as acquired by digital camera sensors are an active area of research which has applications in colour correction [2, 5, 6, 18], camera simulation [10] and sensor design [4].

To capture and reproduce colours so as to achieve perceptual accordance between the scene and the observation by the viewer is not a straightforward task. Digital cameras comprise three kinds of spectral broad-band colour sensors which provide responses for the three colour channels, i.e. red (R), green (G) and blue (B). In practice, these spectral broadband sensors are not colorimetric. This implies

that the RGB values yielded by the camera are not a linear combination of the device-independent CIE colour matching functions [3]. Further, colours, as acquired by digital cameras, are device dependent and can be highly non-linear with respect to the CIE-XYZ colour gamut [20].

Whereas colorimetry focuses on the accuracy of the colours acquired by the camera, spectroscopy studies the spectrum of light absorbed, transmitted, reflected or emitted by objects and illuminants in the scene. In contrast with trichromatic sensors, multispectral and hyperspectral sensing devices can acquire wavelength-indexed reflectance and radiance data in tens of hundreds of bands across a broad spectral range. Moreover, making use of photogrammetry and spectroscopy techniques, it is possible to recover the spectral response of the camera under study [16]. This spectral response, together with material reflectance and illuminant radiance measurements, can be used to perform colorimetric simulations and comparisons.

In this paper, we show how camera simulation and comparison can be effected with respect to the CIE-1931 colour standard. Here, we use the spectral response of the camera to recover the RGB values corresponding to colours, illuminants and materials whose spectrum is known. We have compared these RGB values to those computed making use of the colour matching functions proposed by Stiles and Burch [14, 15].

Thus, we commence by showing how the colour captured by trichromatic cameras can be estimated. We also elaborate on how object colour can be simulated based upon reflectance models. We then present results on three experimental vehicles for three different commercially available cameras. Firstly, we perform simulations using the Planckian formula for the spectrum of light emitted by black body radiators [9]. Secondly, we turn our attention to the results yielded using the spectra of sample colours from the MacBeth Colour Chart. Finally, we present rendering computed using the spectra of skin and plant leaves with sunlight as the illuminant.

---

\*National ICT Australia is funded by the Australian Government's Backing Australia's Ability initiative, in part through the Australian Research Council.

## 2 Colour Estimation

The factors influencing how colour appears on the image are related to the reflecting properties of the materials being observed, the light illuminating the scene and the colour sensor responses of the camera. The surface material and geometry determine the spectral reflectance distribution  $S(\lambda)$  at each wavelength  $\lambda$ . In a similar fashion, the illuminant is characterized by the spectral radiance  $L(\lambda)$ , which describes the emission of the light source as a function of the wavelength  $\lambda$ . Recall that, in here, we focus on the simulation and evaluation of digital cameras, which have a broad spectral response at each of the three colour sensors, i.e. R, G and B, whose spectral sensitivity to the energy incident on the camera image plane as a function of the wavelength  $\lambda$  is denoted by  $C_R(\lambda)$ ,  $C_G(\lambda)$  and  $C_B(\lambda)$ , respectively.

With these ingredients, the photometric process is summarized as follows. A fraction of the light incident on the surface of the object being observed is reflected towards the camera. The light then passes through the camera lens, which focuses the incoming light beam onto the image plane of the camera. Finally, the R, G, B values for each pixel in the image are determined by the responses of the R, G, B receptors of the camera to the incoming light.

### 2.1 Reflectance Models

To simulate and compare the responses of the colour receptors of the camera, a reflectance model is required to relate the geometry of the reflection process to the intrinsic optical properties of the object under study. The modelling of surface reflectance is a topic of pivotal importance, and has hence attracted considerable effort in both, computer vision and computer graphics communities. Reflectance models can be roughly divided into those that are empirical [8, 12], physics-based [1] and phenomenological [11] in nature. Among the physics-based ones, perhaps the Beckmann and Spizichino model [1] for smooth and rough surfaces is the most popular in the graphics and vision communities. However, it relies on the evaluation of the Kirchoff integral and, as a result, it is intractable in closed form. Further, it breaks down when either the surface roughness or the scattering angle is large.

Here, we are interested in simulating surface and subsurface scattering. In practice, light scattered from many natural multi-layered surfaces, including human skin and plant tissue, is composed of a large subsurface scattering component due to reflection at the lower surface boundaries and refraction through translucent layers. Therefore, a physics-based reflectance model that accounts for refractive attenuation of incident light is most appropriate for estimating the colours of these surfaces. For rendering purposes, we

have chosen to incorporate into our simulation method the variant of the Beckmann model proposed by Ragheb and Hancock [13]. This model combines wave scattering theory with a Fresnel correction term [19] to represent the refraction of light through the top surface boundary.

The model in [13] makes use of two physical parameters. The first of these is the standard deviation  $\sigma$  of the height variation with respect to a mean surface level. Secondly, the surface correlation length  $\tau$  characterizes the relative horizontal spacing of the microfacets on the object's surface. This parameter is defined by a surface correlation function of surface height variation for all the points enclosed in a circle with radius  $\tau$ .

As in other reflectance models, the refraction geometry is defined with respect to a local coordinate system whose z-axis is aligned to the local surface normal and whose origin is the point of interest on the surface. The incident light direction is defined by the zenith and azimuth angles  $\theta_i$  and  $\phi_i$ , respectively. The zenith and azimuth angles of the outgoing, i.e. viewer's direction, are  $\theta_s$  and  $\phi_s$ . For the sake of simplicity, we assume that the incident light is always in the  $xz$ -plane, i.e.  $\phi_i = \pi$ . The geometry above is illustrated in Figure 1.

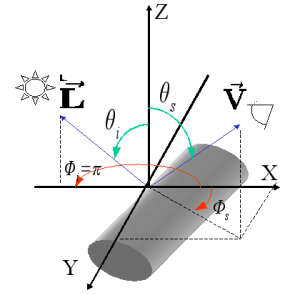


**Figure 1.** Geometry of the reflection process

To commence, we note that, from [13], the mean scattered power from a surface is

$$P(\theta_i, \phi_i = \pi, \theta_s, \phi_s) = \rho_0^2 e^{-g} + D(\theta_i, \phi_i = \pi, \theta_s, \phi_s) \quad (1)$$

where the first term on the right-hand side of the equation above represents the scattering component in the specular direction and the second term is the diffuse scattering component. Let the surface area about the point of interest be  $A = XY$ , where  $X$  and  $Y$  are the width and length of a rectangular patch on the surface under study. With these ingredients, the scattering coefficient  $\rho_0$  of the surface is given by  $\rho_0 = \text{sinc}(v_x X) \text{sinc}(v_y Y)$ , where  $\text{sinc}(x) = \sin(x)/x$ ,  $v_x = k(\sin\theta_i - \sin\theta_s \cos\phi_s)$ ,  $v_y = -k \sin\theta_s \sin\phi_s$ . Here,  $k$  is the propagation rate of the incident light, related to its wavelength  $\lambda$  through the equation  $k = \frac{2\pi}{\lambda}$ .

To simulate surface colours, we assume that the surface correlation function is Gaussian. Given this assumption, it can be shown that the diffuse component for a surface with

a roughness factor  $g$  is

$$D(\theta_i, \phi_i = \pi, \theta_s, \phi_s) = \frac{\pi\tau^2}{A} G_{FC}^2 e^{-g} \sum_{n=1}^{\infty} \frac{g^n}{n!n} e^{-\frac{\tau^2}{4n} v_{xy}^2} \quad (2)$$

where  $g = \sigma^2 v_z^2$ ,  $v_z = -k(\cos(\theta_i) + \cos(\theta_s))$ ,  $v_{xy}^2 = v_x^2 + v_y^2$  and  $G_{FC}$  is a geometric attenuation term.

First, we turn our attention to the term  $G_{FC}$ . Later in the section, we elaborate further on the roughness factor  $g$ . Here, we use the approach of Ragheb and Hancock [13], where the geometric attenuation factor in the Beckmann model is replaced with that derived by Wolff [19]. Thus, the attenuation term becomes

$$G_{FC}^2 = (1 - F(\theta_i, n)) \left(1 - F\left(\arcsin\left(\frac{\sin(\theta_s)}{n}\right), \frac{1}{n}\right)\right) \cos(\theta_i) \quad (3)$$

where  $F(\cdot)$  is a Fresnel function given by

$$F(\theta_i, n) = \frac{1}{2} \left( \frac{\sin(\theta_i - \theta_t)}{\sin(\theta_i + \theta_t)} \right)^2 \times \left( 1 + \left( \frac{\cos(\theta_i + \theta_t)}{\cos(\theta_i - \theta_t)} \right)^2 \right)$$

and  $\theta_t$  is the refractive transmission angle of light into the surface, determined by the Snell's law, i.e.  $\theta_t = \arcsin(\sin(\theta_i)/n)$ . In the expression above,  $n$  is the refractive index of the surface material.

For the sake of simplicity and computational efficiency, we follow [13] and divide the computation of  $D(\cdot)$  into three different cases dependent on the value of the roughness term  $g$ . These are slightly rough, i.e.  $g \ll 1$ , moderately rough, i.e.  $g \simeq 1$ , and very rough, i.e.  $g \gg 1$ . When the surface is rough or very rough, i.e.  $g \gg 1$ ,  $D(\cdot)$  is approximated by

$$D(\theta_i, \phi_i = \pi, \theta_s, \phi_s) = \frac{\pi\tau^2 G_{FC}^2}{A\sigma^2 v_z^2} \exp\left(-\frac{\tau^2 v_{xy}^2}{4\sigma^2 v_z^2}\right) \quad (4)$$

Note that, if the surface is moderately rough, i.e.  $g \simeq 1$ ,  $D(\theta_i, \phi_i = \pi, \theta_s, \phi_s)$  can be approximated with a finite number of terms of the infinite sum in Equation 2. Further, for cases in which the surface is slightly rough, the diffuse component can be approximated by the first term of the summation in Equation 2, i.e.

$$D(\theta_i, \phi_i = \pi, \theta_s, \phi_s) = \frac{\pi\tau^2 G_{FC}^2 g}{A} \exp\left[-\left(g + \frac{v_{xy}^2 \tau^2}{4}\right)\right]$$

## 2.2 Colour Estimation

Having presented the reflectance model employed in this paper, we now proceed to model the RGB responses of the camera sensors. To do this, we depart from the bidirectional reflectance distribution function (BRDF)  $f(\theta_i, \phi_i, \theta_s, \phi_s)$ , which is given by the ratio of the surface radiance  $E_o$  in the

direction  $(\theta_s, \phi_s)$  to the irradiance  $E_i$  falling on the surface in the direction  $(\theta_i, \phi_i)$  [7]. Note that the BRDF is dependent on the light wavelength  $\lambda$ , i.e.

$$f(\theta_i, \phi_i, \theta_s, \phi_s, \lambda) = \frac{E_o(\theta_i, \phi_i, \theta_s, \phi_s, \lambda)}{E_i(\theta_i, \phi_i, \lambda)} \quad (5)$$

To compute the irradiance, we consider the incident energy in the direction  $(\theta_i, \phi_i)$ , which arrives at an infinitesimal patch with a differential solid angle  $d\omega$  on the unit sphere centered at the point of interest in the surface. Since the patch is an infinitesimal area, the light radiance  $L(\lambda)$  is almost constant over this patch. Thus, the energy flux per unit area perpendicular to the light direction can be written as  $L(\lambda)d\omega$ . Since the irradiance onto the surface is measured per unit projected horizontal area, we have

$$E_i(\theta_i, \phi_i, \lambda) = L(\lambda) \cos(\theta_i) d\omega \quad (6)$$

where  $\cos(\theta_i)$  accounts for the ratio of a foreshortened area in the direction  $(\theta_i, \phi_i)$  to the corresponding projected horizontal area.

The BRDF  $f(\theta_i, \phi_i, \theta_s, \phi_s, \lambda)$  can also be viewed as the product of the surface reflectance and the mean scattered power  $P(\theta_i, \phi_i = \pi, \theta_s, \phi_s)$ , as presented in the previous section. Note that, using spectroscopy techniques, the surface reflectance  $S(\lambda)$  for the object material can be measured such that the incident light and viewing directions are perpendicular to the surface. Using this setting, the diffuse scattering of light is governed solely by the surface geometry. Furthermore, the scattering coefficient established by Equation 1 is the attenuation factor of light energy scattered in the viewer's direction. Thus, we have

$$f(\theta_i, \phi_i = \pi, \theta_s, \phi_s, \lambda) = P(\theta_i, \phi_i = \pi, \theta_s, \phi_s) S(\lambda) \quad (7)$$

Combining Equations 5, 6 and 7 yields the surface radiance

$$E_o(\theta_i, \pi, \theta_s, \phi_s, \lambda) = P(\theta_i, \pi, \theta_s, \phi_s) S(\lambda) L(\lambda) \cos(\theta_i) d\omega \quad (8)$$

By assuming that the camera lens has unit transmittance, i.e. the flux radiated from the surface is transmitted through the lens without any loss of energy, the irradiance on the image plane is given by [7]

$$\begin{aligned} I_{im}(\lambda) &= E_o(\theta_i, \pi, \theta_s, \phi_s, \lambda) \frac{\pi}{4} \left(\frac{d}{z}\right)^4 \cos(\alpha)^4 \quad (9) \\ &= m P(\theta_i, \pi, \theta_s, \phi_s) S(\lambda) L(\lambda) \cos(\theta_i) \cos(\alpha)^4 d\omega \end{aligned}$$

where  $m = \frac{\pi}{4} \left(\frac{d}{z}\right)^4$ ,  $d$  is the lens diameter,  $z$  is the focal distance for the lens and  $\alpha$  is the angle between the optical axis of the camera and the ray from the surface patch to the center of the lens.

Since we are interested in the chromaticity rather than the intensity of the light reflected from the surface, we focus our attention on the relative spectral distribution of radiance across wavelengths as an alternative to the absolute radiance value. Note that  $m$  only depends on the camera geometry and, hence, it is constant with respect to the spectral and angular variables of the image irradiance equation. Also, note that the algorithm applies equally to each of the three colour channels and, thus, here we limit our attention to a single colour channel indexed by  $c \in \{R, G, B\}$ . With these ingredients, the response for the colour sensor is given by

$$\begin{aligned} I_c &= \kappa_c \int_V C_c(\lambda) I_{im}(\lambda) d\lambda \\ &= m\kappa_c \cos(\theta_i) d\omega \cos(\alpha)^4 \times \\ &\quad \int_V C_c(\lambda) P(\theta_i, \pi, \theta_s, \phi_s) S(\lambda) L(\lambda) d\lambda \end{aligned} \quad (10)$$

where  $V = [380nm, 780nm]$  is the human visible spectrum.

Note that the value of  $\kappa_c$  in Equation 10 corresponds to the colour balance factor of the camera against a predetermined reference. If a white reference is used, these become the white balance factors. By balancing, the values of  $I_B$ ,  $I_G$  and  $I_R$  are scaled such that a smooth surface, with unit reflectance  $S(\lambda) = 1$  and unit scattering  $P(\cdot) = 1$ , placed perpendicular to the camera axis, i.e.  $\theta_i = \theta_s = \alpha = 0$ , presents a colour perceptually consistent with the reference colour  $s_c$ . Thus, the primary of the colour reference is given by

$$s_c = m\kappa_c d\omega \int_V C_c(\lambda) L(\lambda) d\lambda \quad (11)$$

By solving the equation above for  $\kappa_c$  and substituting into Equation 10, we get

$$\begin{aligned} I_c &= s_c \cos(\theta_i) \cos(\alpha)^4 \times \\ &\quad \frac{\int_V C_c(\lambda) P(\theta_i, \pi, \theta_s, \phi_s) S(\lambda) L(\lambda) d\lambda}{\int_V C_c(\lambda) L(\lambda) d\lambda} \end{aligned} \quad (12)$$

### 3 Experiments

With the expression for the sensor response at hand, we perform experiments on three experimental vehicles. The first of these is the estimation of the colour of a Planckian the blackbody radiator [9] heated at various temperatures. The second set of experiments relates to standard colour indices commonly used for colour correction and calibration in digital photography. Finally, we illustrate how the theory above can be used for rendering purposes.

For our experiments, we have used three camera models. These are the Canon 10D, the Nikon D70 and the Kodak DCS420 models. Note that the Kodak DCS420 is a

discontinued model dating from the mid-nineties whose capacity to accurately capture colour is expected to be outperformed by the Nikon D70 and the Canon 10D. Nonetheless, we have included the Kodak DCS420 as a matter of comparison and validation with the work on spectral sensitivity function measurement in [16, 17].

To assess the fidelity of the colours produced by these cameras, we compare their simulated output with the standard XYZ colours recovered using the colour matching functions in [14, 15], the spectral surface reflectance and the light source radiance measured with a StellarNet spectrometer. As a common practice, for comparison purposes, we choose to plot the colours yielded by the camera spectral sensitivity functions and the colour matching functions on the CIE 1931 colour gamut [3]. To this end, we convert the RGB values into the CIE-XYZ colour space using the following linear transformation

$$\begin{pmatrix} X \\ Y \\ Z \end{pmatrix} = \begin{pmatrix} 0.4124 & 0.3576 & 0.1805 \\ 0.2126 & 0.7152 & 0.0722 \\ 0.0193 & 0.1192 & 0.9505 \end{pmatrix} \begin{pmatrix} R \\ G \\ B \end{pmatrix} \quad (13)$$

To recover the spectral sensitivity function for the cameras under study, we use a procedure akin to that in [16, 17]. Narrow band illumination is obtained by passing light from a calibrated tungsten source through an OKSI Liquid Crystal Tunable filter. This narrow band light is used to image an ASD LabSphere Spectralon white reference. For photometric calibration purposes, we measure the spectrum of the narrow band illuminant on the white reference making use of a StellarNet spectrometer whose probe is placed at a similar geometric configuration with respect to the white reference as that of the camera. In Figure 2 we show the colour matching functions and the spectral sensitivity functions for the Canon 10D, the Nikon D70 and the Kodak DCS420. It is worth noting that the spectral sensitivity functions for the Kodak DCS420 camera are consistent with those reported in [16, 17].

#### 3.1 Colour Temperature

As mentioned earlier, we first examine the colour temperature as a characteristic of a Planckian illuminant, where the colour temperature of an illuminant is given by its chromaticity as compared with a heated black body radiator. The temperature in Kelvin at which the chromaticity of the black body radiation is equivalent to that of the illuminant under consideration is its colour temperature. Colour temperature has applications in photography and is relevant to white balancing of digital cameras. Further, it has been used as a standard benchmark in colorimetry [20].

The spectral radiant exitance per unit surface area per unit solid angle for a black body radiator is governed by

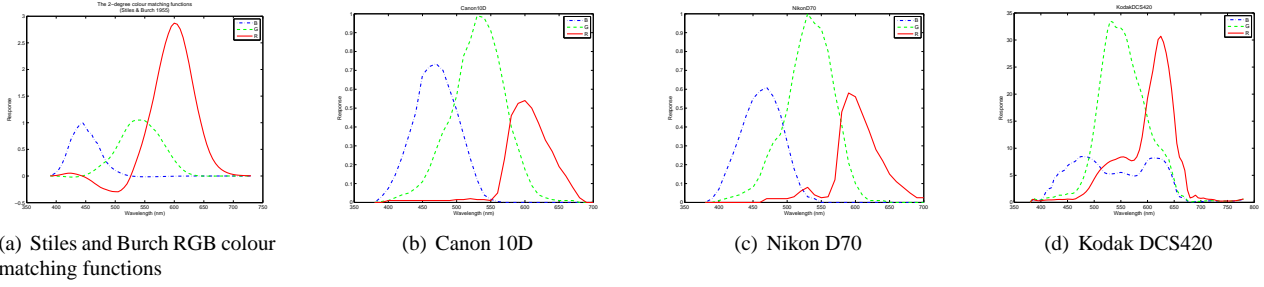


**Figure 2.** Left-hand panel: Stiles and Burch RGB colour matching functions; Middle and right-hand panels, from left-to-right: RGB sensitivity functions for the Canon 10D, the Nikon D70 and Kodak DCS420 cameras.

Planck's law. As a function of wavelength, Planck's law is given by

$$E_{bb}(\lambda, T) = \frac{c_1}{\lambda^5 (e^{c_2/(\lambda T)} - 1)} \quad (14)$$

where  $T$  is the temperature in Kelvin,  $\lambda$  is the wavelength variable as before and  $c_1 = 3.74183 \times 10^{-16} Wm^2$  and  $c_2 = 1.4388 \times 10^{-2} mK$  are constants.

Making use of the spectral radiant exitance, the colour temperature captured by the camera can be computed by using  $E_{bb}(\lambda, T)$  as an alternative to the image irradiance  $I_{im}(\lambda)$ . Note that the colour temperature is determined by the illuminant chromaticity. As a result, we can use Equation 12 to determine the colour temperature by assuming

that the RGB spectral sensitivity functions of the camera are normalized to unity, i.e.  $s_R = s_G = s_B = 1$ , against a white colour reference with unit reflectance  $S(\lambda) \equiv 1$ . Moreover, if the incident light and viewer's direction are aligned with the surface normal and the optical axis of the camera, we can simplify Equation 12 so as to obtain the colour of the blackbody radiator at temperature  $T$  by

$$\begin{aligned} I_B(T) &= \frac{\int_V C_B(\lambda) E_{bb}(\lambda, T) d\lambda}{\int_V C_B(\lambda) d\lambda} \\ I_G(T) &= \frac{\int_V C_G(\lambda) E_{bb}(\lambda, T) d\lambda}{\int_V C_G(\lambda) d\lambda} \\ I_R(T) &= \frac{\int_V C_R(\lambda) E_{bb}(\lambda, T) d\lambda}{\int_V C_R(\lambda) d\lambda} \end{aligned} \quad (15)$$

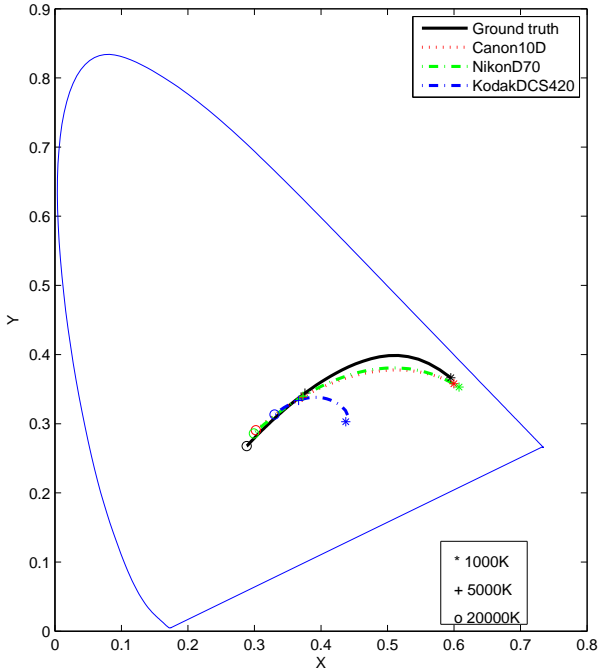


**Figure 3.** Estimated colour temperature for the range  $[1000^\circ K, 20000^\circ K]$  corresponding to the three camera models and the ground truth.

In Figure 3 we show a plot on the CIE-XYZ gamut of the colour temperatures for a black body radiator heated at temperatures ranging from  $1000^\circ K$  to  $20000^\circ K$ . Each curve corresponds to the colour temperature yielded by each camera as compared with those obtained using the colour matching functions, which we use as ground truth for our experiments.

Note that, from the figures, the curves in the temperature range of  $[5000^\circ K, 6200^\circ K]$  for the three cameras are in good accordance to that yielded by the colour matching functions. This implies that all the cameras under evaluation are able to perform appropriate white balancing against natural sunlight. Further, the length of each curve across the gamut indicates the dynamic range of the corresponding camera. In particular, the dynamic range of Kodak DCS420 camera is shorter than those of the others. The second observation is that the Canon 10D and Nikon D70 curves are closer to the ground truth than the Kodak DCS420 curve. In the cases where the colour temperature is close to its extreme values, the colour produced by Kodak DCS420 is considerably different from those produced by the other two cameras.

### 3.2 Colour Simulation

Our second experimental vehicle focuses on the estimation of colours from the MacBeth Colour Checker. This is a chart that provides a set of known colours commonly used for colour correction and white balance setup. Here we have used a subset of colours from the chart. These are Red (C1), Green (C2), Blue (C3), White (C4) and Orange Yellow (C5). For purposes of simulation, we measure the reflectance of each of the colour patches under study making use of a StellarNet spectrometer so as to obtain the spectra in the range between 380 and 780 nm. The reflectance spectra of the colours under study are shown in Figure 4.

Given the reflectance spectrum for each colour patch, we estimate the RGB response for the sensors in each camera and compare them with those yielded by the colour matching functions [14, 15], which we use as ground truth. Since, ideally, the estimated surface colour should be independent of the illuminant colour, the illumination spectrum is set to unity, i.e.  $L(\lambda) = 1$ , for all  $\lambda \in [380nm, 780nm]$ . With similar assumptions as those used in the previous section, the RGB values of the colour patch under study are estimated by the equation

$$\begin{aligned} I_B &= \frac{\int_V C_B(\lambda)S(\lambda)d\lambda}{\int_V C_B(\lambda)d\lambda} \\ I_G &= \frac{\int_V C_G(\lambda)S(\lambda)d\lambda}{\int_V C_G(\lambda)d\lambda} \\ I_R &= \frac{\int_V C_R(\lambda)S(\lambda)d\lambda}{\int_V C_R(\lambda)d\lambda} \end{aligned} \quad (16)$$

where  $S(\lambda)$  is the measured spectral reflectance of the

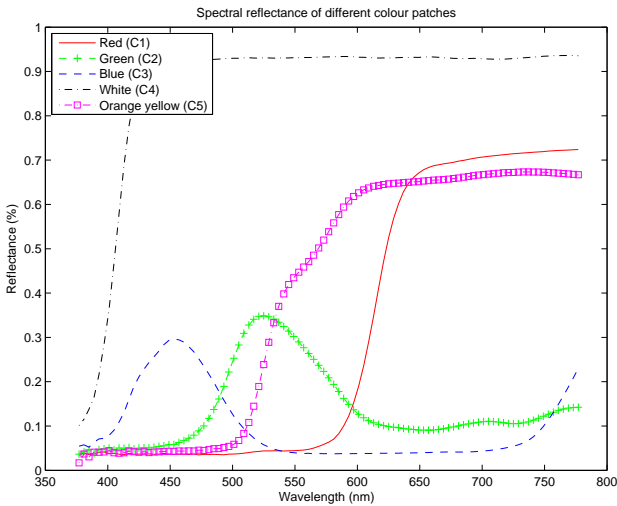


**Figure 4.** Reflectance spectra for the five colour patches. From left-to-right: Red (C1), Green (C2), Blue (C3), White (C4) and Orange Yellow (C5).

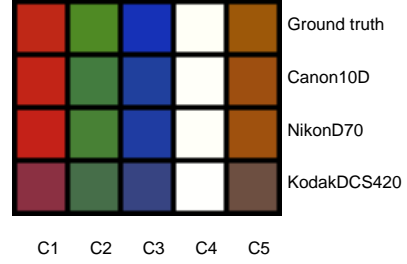


**Figure 5.** The colours observed by the three cameras and the ground truth.

colour patch. Finally, the estimated RGB colour is transformed into the CIE-XYZ colour space by Equation 13.

In Figure 5, we show the estimated colours in the form of a chart indexed according to camera and colour of reference. Note that the estimated RGB value for the patch C4 (White) is the same for the the three cameras and the colour matching functions. This is not surprising and follows from the equations above. If the reflectance spectrum is unity across the visible spectrum, i.e.  $S(\lambda) = 1$  for all  $\lambda \in [380nm, 780nm]$ , the RGB values are unity. In Figure 5, the Canon 10D and Nikon D70 achieve a colour estimate close to the ground truth for patch C1 (Red) and patch C5 (Orange Yellow). Also, the resulting Green (C2) and Blue (C3) colours yielded by these cameras are perceptually distinguishable from the ground truth. The Kodak DCS420 camera produces colours which are distinct from those of

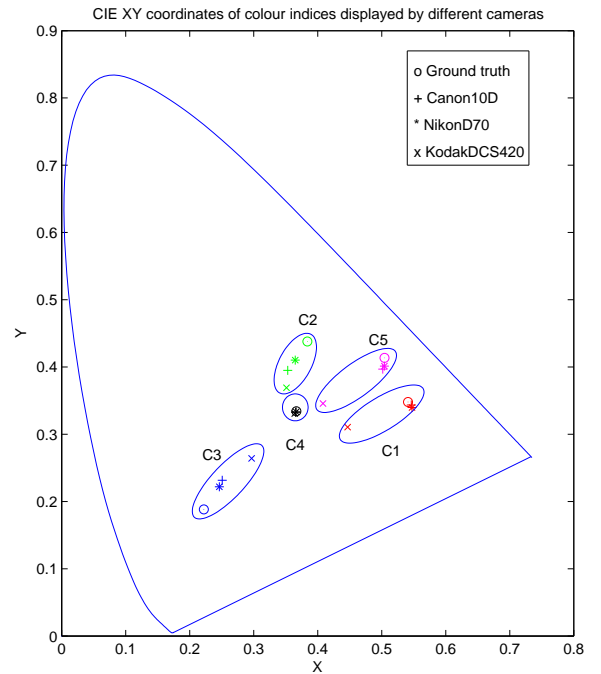


**Figure 6.** CIE-XYZ plots for the five colours under study.

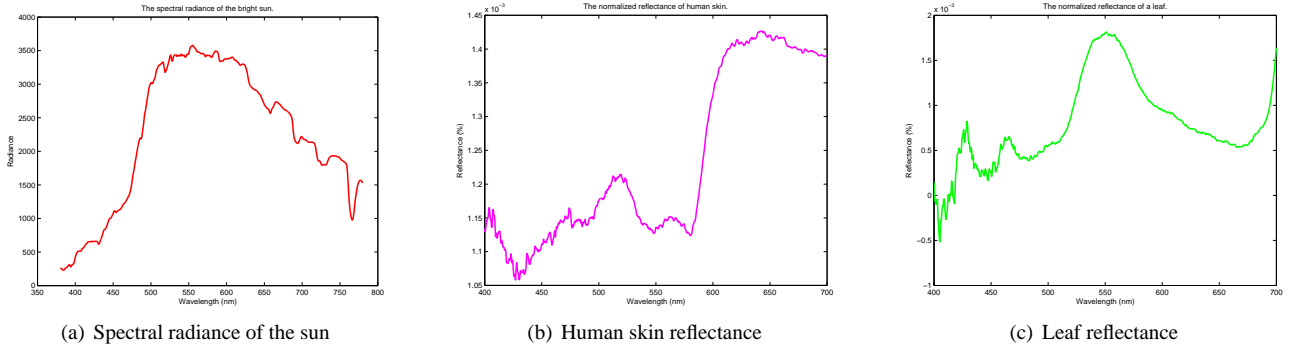


**Figure 7.** From left-to-right: Radiance of the sun (7(a)) and spectral reflectance of human skin (7(b)) and a plant leaf (7(c)).

the other cameras and the ground truth.

In a more quantitative study, we plot in Figure 6 the simulated colours under study for the three camera models and the ground truth on the CIE-XYZ gamut. Each cluster in the figure corresponds to a different colour. Note that the qualitative results in Figure 5 agree with those in Figure 6. The Red (C1) and Orange Yellow (C5) points for the Canon 10D and Nikon D70 cameras are close to those yielded by the colour matching functions, while the Green (C2) and Blue (C3) coordinates for these two cameras are further apart from the ground truth. This result, again, reinforces the notion that the Canon 10D and Nikon D70 cameras can produce Red and Orange Yellow shades more accurately than Green and Blue ones. Also, the Kodak DCS420 response curves produce colour point-coordinates that are well separated from the others in each of the C1, C2, C3 and C5 clusters. This agrees with both, our qualitative analysis and the results yielded by our colour temperature experiments.

### 3.3 Mesh Rendering

In this section, we demonstrate the utility of the simulation method presented here for purposes of simulating the appearance of 3D meshes whose image has been acquired making use of the digital cameras under study. To this end, we have used a fern and a human head. These meshes can be viewed as a collection of planar polygons whose RGB colour is determined by Equation 12.

For purposes of rendering, the illuminant in the scene is considered to be a point light source. Here, the radiance  $L(\lambda)$  of the illuminant is given by the sunlight spectrum. The surface reflectance spectra used here are those of human skin for the head and a plant leaf for the fern. These were measured using a StellarNet spectrometer. In Figure 7(a), we show the spectra used in our experiments. For white balancing, we have assumed a CIE D55 colour temperature ( $5500^\circ$  K). At a colour temperature of  $5500^\circ$  K, the  $s_R : s_G : s_B$  proportion for the computation in Equation 12 is  $1.1040 : 0.9870 : 0.8233$ .

In our implementation, the mean scattered power  $P(\cdot)$

in Equation 12 is computed for the mesh polygons adjacent to the vertex of reference. The tangent plane at each vertex is the one perpendicular to the local surface normal. This plane is used as the mean surface level when computing the height variation standard deviation  $\sigma$ . For a specific wavelength  $\lambda$  of incident light, the roughness level of the local area around a vertex is determined by the value of  $g = \sigma^2 v_z^2$ . The approximation presented in Section 2.1 is used to compute the mean scattered power of the surface patch.

Figure 8 presents the rendering of the head yielded using the camera spectral sensitivity functions and the Stiles and Burch’s colour matching functions. The Canon 10D and the Nikon D70 produce results that closely resemble the one computed using the colour matching functions. The colour achieved by the Kodak DCS420 camera has a higher saturation and tends further to the white, which makes the head appear slightly brighter.

Similarly, in Figure 9, we show the rendering for the fern plant with the reflectance of a leaf. The surface colour rendered with the Kodak DCS420 response curves is closer to the white reference than that yielded by the Canon 10D and Nikon D70 cameras. The latter response curves produce rendering with a stronger green component, which looks more natural than that of the Kodak camera. However, in contrast with the results shown in Figure 8, the simulation for these two cameras is perceptually different from that computed making use of the RGB colour matching functions.

## 4 Conclusion

In this paper, we have presented a digital camera evaluation and comparison method based upon photogrammetry, colorimetry and spectroscopy. The method is quite general in nature and applies to a wide variety of trichromatic digital cameras commercially available. Moreover, we have presented results involving Planckian illuminants, colour calibration charts and meshes rendered using spectroscopic measurements. These results are relevant to areas such as



**Figure 8.** Rendering of a head with the skin reflectance of a Caucasian male under bright sunlight; From left-to-right: results yielded by the Stiles and Burch’s colour matching functions, the Canon 10D, Nikon D70 and Kodak DCS420 cameras.

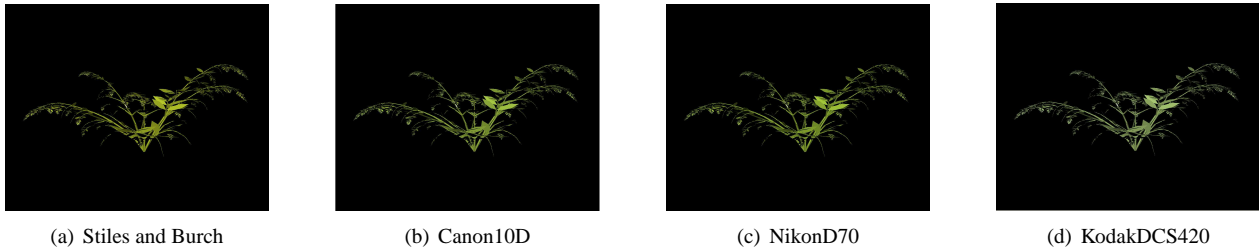


**Figure 9.** Rendering of a fern with the reflectance of a leaf under sunlight. From left-to-right: rendering yielded by the Stiles and Burch’s colour matching functions, the Canon 10D, Nikon D70 and Kodak DCS420 cameras.

white balancing, colour correction and photorealistic rendering.

## References

- [1] P. Beckmann and A. Spizzichino. *The Scattering of Electromagnetic Waves from rough Surfaces*. Pergamon Press, 1963.
- [2] D. H. Brainard. *Colorimetry*. McGraw-Hill, 1995.
- [3] CIE. *Commission Internationale de l’Éclairage Proceedings, 1931*. Cambridge University Press, Cambridge, 1932.
- [4] T. Ejaz, T. Horiuchi, G. Ohashi, and Y. Shimodaira. Development of a camera system for the acquisition of high-fidelity colors. E89–C(10):1441–1447, 2006.
- [5] G. D. Finlayson and M. S. Drew. The maximum ignorance assumption with positivity. In *Proceedings of the IS&T/SID 4th Color Imaging Conference*, pages 202–204, 1996.
- [6] B. K. P. Horn. Exact reproduction of colored images. *Computer Vision, Graphics, and Image Processing*, 26(135), 1981.
- [7] B. K. P. Horn. *Robot Vision*. MIT Press, Cambridge, Massachusetts, 1986.
- [8] E. P. F. Lafortune, S.-C. Foo, K. E. Torrance, and D. P. Greenberg. Non-linear approximation of reflectance functions. In *SIGGRAPH ’97: Proceedings of the 24th annual conference on Computer Graphics and Interactive Techniques*, pages 117–126, New York, USA, 1997.
- [9] H.-C. Lee. *Introduction to Color Imaging Science*. University Press, Cambridge, UK, 2005.
- [10] P. Longere and D. H. Brainard. Simulation of digital camera images from hyperspectral input. In C. van den Branden Lambrecht, editor, *Vision Models and Applications to Image and Video Processing*, pages 123–150. Kluwer, 2001.
- [11] M. Oren and S. K. Nayar. Generalization of the lambertian model and implications for machine vision. *International Journal of Computer Vision*, 14(3):227–251, April 1995.
- [12] B. T. Phong. Illumination for computer generated pictures. *Commun. ACM*, 18(6):311–317, 1975.
- [13] H. Ragheb and E. R. Hancock. Testing new variants of the Beckmann-Kirchhoff model against radiance data. *Computer Vision and Image Understanding*, 102(2):145–168, May 2006.
- [14] W. S. Stiles and J. M. Burch. Interim report to the Commission Internationale de l’Éclairage Zurich, 1955, on the National Physical Laboratory’s investigation of colour-matching. *Optica Acta*, 2:168–181, 1955.
- [15] W. S. Stiles and J. M. Burch. N.P.L. colour-matching investigation: Final report (1958). *Optica Acta*, 6:1–26, 1959.
- [16] P. Vora, J. Farrell, J. Tietz, and D. Brainard. Digital color cameras – 2 – spectral response. Technical Report HPL-97-54, HP Laboratories, March 1997.
- [17] P. Vora, J. Farrell, J. Tietz, and D. Brainard. Image capture: simulation of sensor responses from hyperspectral images. *IEEE Transactions on Image Processing*, 10(2):307–316, February 2001.
- [18] B. A. Wandell. The synthesis and analysis of color images. *IEEE Transactions on Pattern Analysis and Machine Intelligence*, 9(1):2–13, 1987.
- [19] L. B. Wolff. Diffuse-reflectance model for smooth dielectric surfaces. *Journal of the Optical Society of America*, 11(11):2956–2968, November 1994.
- [20] G. Wyszecki and W. Stiles. *Color Science: Concepts and Methods, Quantitative Data and Formulae*. Wiley, 2000.